

Towards higher electro-optic response in AlScN

Haochen Wang,¹ Sai Mu,² and Chris G. Van de Walle¹

¹⁾*Materials Department, University of California Santa Barbara, Santa Barbara, CA 93106, USA*

²⁾*Department of Physics and Astronomy, University of South Carolina, Columbia, SC 29208, USA*

(*Electronic mail: vandewalle@mrl.ucsb.edu)

(*Electronic mail: mus@mailbox.sc.edu)

(Dated: 11 October 2024)

Novel materials with large electro-optic (EO) coefficients are essential for developing ultra-compact broadband modulators and enabling effective quantum transduction. Compared to lithium niobate, the most widely used nonlinear optical material, wurtzite AlScN offers advantages in nano-photonic devices due to its compatibility with integrated circuits. We perform detailed first-principles calculations to investigate the electro-optic effect in $\text{Al}_{1-x}\text{Sc}_x\text{N}$ alloys and superlattices. At elevated Sc concentrations in alloys, the EO coefficients increase; importantly, we find that cation ordering along the *c* axis leads to enhanced EO response. Strain engineering can be used to further manipulate the EO coefficients of AlScN films. With applied in-plane strains, the piezoelectric contributions to the EO coefficients increase dramatically, even exceeding 251 pm/V. We also explore the possibility of EO enhancement through superlattice engineering, finding that nonpolar *a*-plane $(\text{AlN})_m/(\text{ScN})_n$ superlattices increase EO coefficients beyond 40 pm/V. Our findings provide design principles to enhance the electro-optic effect through alloy engineering and heterostructure architecture.

The Pockels electro-optic (EO) effect describes the linear variation in the refractive index of an optical medium in response to an applied electric field.¹ It occurs only in materials without inversion symmetry, unlike the (typically much smaller) Kerr effect,² which is proportional to the square of the electric field. Identifying materials with large EO coefficients has garnered increasing attention due to their potential to enable high-speed and low-power EO modulation in integrated photonics applications^{3–6} and quantum transduction in quantum information science.^{7–11}

In commonly used EO materials such as lithium niobate (LiNbO_3 , LNO),^{12,13} barium titanate^{14–16} and lead titanate¹⁷ large EO coefficients primarily arise from the ionic response due to soft optical phonon modes. However, the difficulty of integrating them with silicon photonics has spurred a search for alternative materials with large EO coefficients.

Aluminum nitride (AlN) has seen increasing use in integrated nano-photonic and opto-mechanical devices due to its excellent compatibility with complementary metal-oxide-semiconductor (CMOS) fabrication.^{18–21} Coherent conversion between microwave and optical photons, based on the electro-optic effect, has been successfully accomplished using optical micro-ring cavities made of AlN.⁷ However, the EO coefficients of AlN are smaller than those in conventional materials such as LNO (30 pm/V²²).

Alloying offers a promising solution to address this limitation while maintaining CMOS compatibility.²³ Introducing scandium (Sc) into AlN modifies the crystal structure, enhances its piezoelectric response and can also lead to ferroelectricity.^{24–27} Strong piezoelectricity and the presence of ferroelectricity are known to contribute to electro-optic coupling.^{14,22} However, quantitative data on the EO coefficients of AlScN is lacking, and the interplay between piezoelectricity and the EO effect is still to be elucidated.

In this paper, we conduct first-principles calculations to the-

oretically investigate the EO coefficients in $\text{Al}_{1-x}\text{Sc}_x\text{N}$ alloys. We find that the increase in the EO coefficient r_{33} with Sc concentration (x_{Sc}) is mainly due to the piezoelectric contribution r_{33}^{piezo} , rather than the clamped term r_{33}^{clamped} . Based on a systematic analysis of alloy configurations we associate large piezoelectric EO coefficients with the presence of cation ordering along the *c* axis, which leads to enhanced compliance constants. We investigate the effect of strain on $\text{Al}_{1-x}\text{Sc}_x\text{N}$ alloys, finding that in-plane strains can significantly enhance EO coefficients, with r_{33} values even exceeding 251 pm/V. We also explore superlattices, which can enhance control over structural features. Nonpolar *a*-plane $(\text{AlN})_m/(\text{ScN})_n$ superlattices are particularly promising, showing an increase in both clamped and piezoelectric EO coefficients with Sc layer thickness and reaching r_{33} values up to 40 pm/V.

All calculations are performed within density functional theory using optimized norm-conserving Vanderbilt pseudopotentials²⁸ and the ABINIT software package.²⁹ Density functional perturbation theory is employed to calculate the electro-optic coefficients.³⁰ The exchange-correlation energy is calculated using the local density approximation (LDA),^{31,32} more accurate functionals, such as hybrid functionals,³³ are currently not implemented in existing software for electro-optic properties. The accuracy of using LDA is addressed in Sec. A of the Supplementary Material (SM). To simulate the disordered environment in $\text{Al}_{1-x}\text{Sc}_x\text{N}$ alloys we use 32-atom supercells which are constructed as $1 \times 2 \times 2$ multiples of the 8-atom orthorhombic unit cell.³⁴ We also use 48-atom supercells to examine whether the size of the supercell impacts the alloy simulations. We find that using 32- and 48-atom supercells leads to almost identical results. We study Sc concentrations from 0 to 50%; at each concentration we generate ten inequivalent configurations by randomly placing Sc atoms on cation sites. A plane-wave cutoff energy of 45 Hartree and a $3 \times 3 \times 2$ Monkhorst-Pack *k*-point grid are

used.³⁵ All structures are fully relaxed until the interatomic forces are smaller than 5×10^{-5} Hartree/Bohr. The physical observables at each Sc concentration are obtained by averaging over the calculated properties of each supercell.

The electro-optic effect is usually introduced in the context of the optical ellipsoid:²

$$\Delta \left(\frac{1}{n_{ij}^2} \right) = \Delta (\epsilon^{-1})_{ij} = \sum_k r_{ijk} E_k, \quad (1)$$

where n_{ij} are the components of the refractive index, E_k the external electric field components, and r_{ijk} the EO coefficients.

The EO tensor can be expressed as the sum of three contributions: bare electronic components r_{ijk}^{elec} , ionic responses r_{ijk}^{ion} and piezoelectric contributions r_{ijk}^{piezo} .³⁰ In the linear response regime, the three contributions are independent and additive ($r_{ijk}^{\text{tot}} = r_{ijk}^{\text{elec}} + r_{ijk}^{\text{ion}} + r_{ijk}^{\text{piezo}}$). The electronic contributions originate from the interaction between the applied electric field and the electron cloud, with ions frozen at their equilibrium positions. The ionic contributions result from E -field-induced atomic relaxation while keeping the electron cloud frozen. The clamped EO coefficients r_{ijk}^{clamped} combine these electronic and ionic contributions while neglecting the contributions from lattice deformations, and are defined as follows:

$$r_{ijk}^{\text{clamped}} = r_{ijk}^{\text{elec}} + r_{ijk}^{\text{ion}} = \frac{-8\pi}{n_i^2 n_j^2} \chi_{ijk}^{(2)} - \frac{4\pi}{n_i^2 n_j^2 \sqrt{\Omega_0}} \sum_m \frac{\alpha_{ij}^m l_{m,k}}{\omega_m^2}. \quad (2)$$

Here $\chi_{ijk}^{(2)}$ represents the second-order optical susceptibility and Ω_0 denotes the cell volume. α_{ij}^m , the Raman susceptibility of phonon mode m , and $l_{m,k}$, the mode polarity³⁶ along the k direction are defined as follows:

$$\alpha_{ij}^m = \sqrt{\Omega_0} \sum_{\kappa, \beta} \frac{\partial \chi_{ij}^{(1)}}{\partial \tau_{\kappa, \beta}} u_m(\kappa \beta), \quad (3)$$

$$l_{m,k} = \sum_{\kappa, \beta} Z_{\kappa, k \beta}^* u_m(\kappa \beta), \quad (4)$$

where $u_m(\kappa \beta)$ denotes the phonon eigendisplacement of atom κ in the β direction of mode m . $\frac{\partial \chi_{ij}^{(1)}}{\partial \tau_{\kappa, \beta}}$ is the derivative of the linear electric susceptibility with respect to atomic displacement, with atom κ moving in the β direction. $Z_{\kappa, k \beta}^*$ is the k -component of the Born effective charge of atom κ moving in the β direction.

The piezoelectric contribution arises from the lattice deformation induced by the electric field, which in turn changes the dielectric constants; it can be computed using the piezoelectric strain coefficients $d_{k\mu\nu}$ and the elasto-optic coefficients $p_{ij\mu\nu}$ (which represent the derivative of the inverse dielectric tensor with respect to the strain):

$$r_{ijk}^{\text{piezo}} = \sum_{\mu, \nu=1}^3 p_{ij\mu\nu} d_{k\mu\nu}. \quad (5)$$

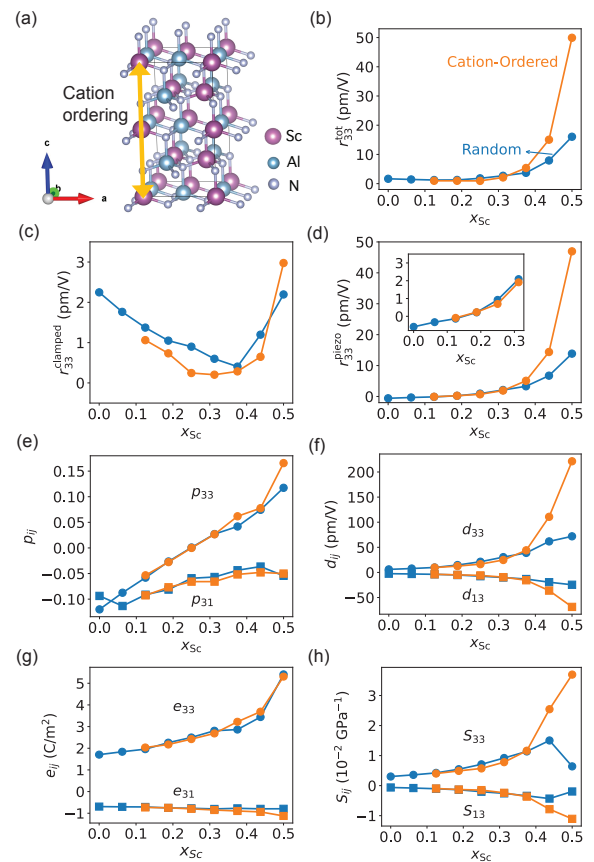


FIG. 1. (a) Atomic structure of a 32-atom supercell of $\text{Al}_{0.5}\text{Sc}_{0.5}\text{N}$. The orange arrow denotes a third-nearest cation-cation neighbor. (b) Total, (c) Clamped and (d) Piezoelectric EO coefficients r_{33} (the inset shows r_{33}^{piezo} at $x_{\text{Sc}} \leq 31.25\%$); (e) Elasto-optic coefficients p_{33} and p_{31} ; (f) Piezoelectric strain coefficients d_{33} and d_{13} ; (g) Piezoelectric stress coefficients e_{33} and e_{31} ; (h) Compliance constants S_{33} and S_{13} . Blue symbols represent averaged values over randomly generated alloy configurations, while orange symbols represent averages over structures with cation ordering along the c axis.

In the subsequent discussion, Voigt notation is adopted. Due to the symmetry of indices i and j , r_{ijk} can be contracted to a 6×3 tensor r_{hk} . Similarly, piezoelectric strain coefficients $d_{k\mu\nu}$ can be represented by a 6×3 tensor and elasto-optic coefficients $p_{ij\mu\nu}$ by a 6×6 tensor. Which components of the tenors are independent and nonzero can be determined by a symmetry analysis of the crystal.

Our actual results at each Sc concentration are obtained by averaging over ten different supercells with randomly placed cations. Calculated lattice parameters a , the c/a ratio, and the internal displacement parameter u are plotted in Fig. S1 (Sec. B in the SM). They compare well with experiments.^{37,38} The phase transition from wurtzite to a metastable layered-hexagonal structure (with $u = 0.5$) occurs between 37.5% and 43.75%, consistent with previous findings.^{27,37,39}

The wurtzite structure has the $6mm$ point group, giving three independent nonzero elements in the EO tensor: r_{13} , r_{33} , and r_{51} . Among these, r_{33} ($=r_{333}=r_{zzz}$), which quantifies the

response of the zz component of the inverse dielectric tensor to the applied field along z , is the largest. A fully disordered solid solution should retain the wurtzite symmetry. However, the finite-size supercells that we use to model the alloy do lower the symmetry, thus introducing additional nonzero elements such as r_{11} and r_{22} . Our calculations indicate that such additional components are small and close to zero when averaging over multiple supercells (see Sec. C in the SM).

The results of our systematic investigation of the EO effect are shown in Fig. 1. For alloy configurations with randomly placed cations (labeled “Random”), r_{33}^{clamped} first decreases with x_{Sc} and then increases, with a turning point roughly corresponding to the phase-transition concentration. In contrast, r_{33}^{piezo} monotonically increases over the entire range of Sc concentrations, starting out smaller than the clamped contribution at low concentrations but significantly contributing to the total r_{33} at concentrations above 30%.

The variations of both clamped and piezoelectric EO coefficients among different configurations of random alloys are small at low x_{Sc} but become significant at high x_{Sc} (see Sec. D in the SM). We now focus on identifying the structural features of alloy configurations that give rise to particularly high EO coefficients, with the goal of providing guidelines for design or synthesis of high-EO materials. Through analyses of pair distribution functions and ruling out the possibility that pairs of cations cause enhancements, we found that a common structural feature gives large EO coefficients, namely the formation of same-species cation chains along the c axis [see Fig. 1(a)]. While we do not aim to address the details of the alloy energetics, we observe that at every concentration the structure with the lowest energy is invariably a cation-ordered structure, rendering their occurrence in experimental samples quite likely. To confirm the correlation of this ordering with enhancements in the EO coefficients, we generate multiple additional cation-ordered configurations at each concentration, deliberately forming same-species chains along the c axis.

The following analysis focuses on r_{33} , but similar results are obtained for r_{13} . In Fig. 1(b), we plot averaged EO coefficients r_{33}^{tot} of random alloys (blue) and cation-ordered structures (orange). The r_{33}^{tot} of cation-ordered structures is significantly more enhanced at high x_{Sc} compared to the random structures. Comparing Fig. 1(c) and (d), this is caused by the enhancement of piezoelectric EO contributions in cation-ordered structures. Using Voigt notation and taking advantage of the wurtzite symmetry in Eq. (5), r_{33}^{piezo} can be written as $r_{33}^{\text{piezo}} = 2p_{31}d_{13} + p_{33}d_{33}$. Figures 1(e) and (f) illustrate the piezoelectric strain coefficients (d_{ij}) and the elasto-optic coefficients (p_{ij}) for both random and cation-ordered structures. We find that (1) p_{33} and d_{33} , increasing faster than p_{31} and d_{13} , dominate the contributions to r_{33}^{piezo} ; (2) p_{33} and p_{31} are relatively insensitive to the details of the structure, given similar results of random and cation-ordered structures; and (3) d_{33} and d_{13} are not sensitive to structure up to $x_{\text{Sc}} = 37.5\%$, but are significantly enhanced in the cation-ordered structures at 43.75% and 50%. We can therefore attribute the enhancement of r_{33}^{piezo} in cation-ordered structures at high x_{Sc} to the rise in piezoelectric strain coefficients d_{33} and d_{13} .

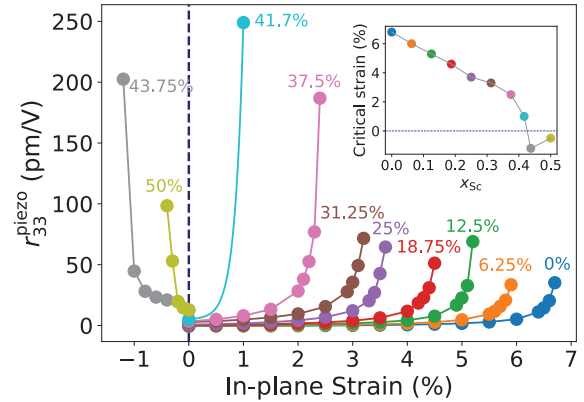


FIG. 2. Piezoelectric EO coefficients r_{33}^{piezo} of $\text{Al}_{1-x}\text{Sc}_x\text{N}$ as a function of in-plane strain (positive for tensile strain, negative for compressive strain). The inset shows the decrease in critical strain⁴² values as a function of Sc concentration x_{Sc} .

We explore the enhancement in more detail by writing the piezoelectric strain coefficients d_{ij} as a product of the piezoelectric stress tensor e_{ik} and the compliance tensor S_{kj} :

$$d_{ij} = \sum_k e_{ik} S_{kj}. \quad (6)$$

Figure 1(g) and (h) show that e_{33} and e_{31} have similar values in random and cation-ordered structures, but S_{33} and S_{13} show significant enhancements in cation-ordered structures at Sc concentrations of 43.75% and 50%. The larger S_{33} values in the cation-ordered structures reflect weaker cation-nitrogen bond strength along the c axis, as confirmed by a crystal orbital Hamilton population analysis^{40,41} (see Sec. E in the SM).

The combination of high Sc content and cation ordering enhances the EO response by pushing the system closer to the phase transition. When we increase the Sc content of random alloys, the in-plane lattice parameter a and the u parameter increase, but the alloys transition from the wurtzite phase to a layered-hexagonal phase (Fig. S1). Cation ordering along the c axis counteracts the effect of rising Sc concentration, reducing both the in-plane lattice parameter a and the u parameter, thus driving the system back to the wurtzite phase and closer to the phase transition.

These insights about the role of Sc concentration and cation ordering suggest that manipulating the lattice parameter by applying in-plane strain could also be fruitful. Due to the mismatch of in-plane lattice parameters, strain is likely to be present in heteroepitaxially grown films, such as $\text{Al}_{1-x}\text{Sc}_x\text{N}$ grown on GaN⁴³ or Si⁴⁴ substrates. Large strain effects on EO coefficients were experimentally and computationally demonstrated in the cases of SrTiO_3 ,^{45,46} strained silicon^{47,48} and c -plane (AlN)₁/(ScN)₁ superlattices.⁴⁹

At each Sc concentration, we select one configuration of the $\text{Al}_{1-x}\text{Sc}_x\text{N}$ random alloy and apply in-plane strain by constraining the in-plane lattice parameters and relaxing the out-of-plane lattice parameter and all internal degrees of freedom. In Sec. F of the SM we demonstrate that our conclusions

regarding strain do not depend on the specific choice of alloy configuration. The results in Fig. 2 show that for x_{Sc} below 43.75%, r_{33}^{piezo} first increases slowly with in-plane *tensile* strains, then dramatically rises as the strain approaches a critical value. However, at higher x_{Sc} (43.75% and 50%), in-plane *compressive* strain is needed to enhance r_{33}^{piezo} .

The difference in the sign of the strain needed for enhancement makes clear that the strain has an impact because it drives the system closer to the phase transition: for wurtzite ($x_{\text{Sc}} \leq 37.5\%$), in-plane *tensile* strain is required to increase u and drive the system towards a layered-hexagonal phase, while for the metastable layered-hexagonal structures ($x \geq 43.75\%$), we need in-plane *compressive* strain to decrease u and push the system back to wurtzite.

In Sec. G of the SM, we analyze the r_{33}^{clamped} and all factors contributing to r_{33}^{piezo} under in-plane strains. Figure S6 shows that r_{33}^{clamped} , p_{33} and e_{33} increase monotonically and almost linearly with strain at x_{Sc} below 43.75%. For r_{33}^{piezo} , its dramatic enhancement near the critical strain mainly originates from the piezoelectric strain coefficients d_{33} and the compliance constants S_{33} .

The inset of Fig. 2 shows that the critical strain decreases as a function of x_{Sc} . This means that a relatively small strain can greatly enhance the EO response in $\text{Al}_{1-x}\text{Sc}_x\text{N}$ alloys with high Sc content. As a test, we modeled a 41.7% alloy (in a 48-atom supercell) and found that a 1% strain suffices to increase r_{33} to 251 pm/V. Achieving strains large enough to make a significant difference at low x_{Sc} may be challenging. We note however, that inhomogeneities in the alloy could lead to locally enhanced Sc concentrations, and potentially local strains as well. Since the strain enhancement is highly nonlinear, it is thus conceivable that significant increases in EO coefficients could be observed in inhomogeneous alloys with nominal Sc concentrations well below the phase transition.

Our finding that the cation ordering along the c axis can magnify the EO coefficients inspires us to design structures that would build in such order. Superlattices offer this potential because they can be grown with atomic precision. Since the relevant cation ordering is along the c axis, we focus on structures in which the c axis lies in the growth plane, which is the case for non-polar a -plane superlattices [Fig. 3(a)].⁵⁰ We perform systematic studies of a -plane $(\text{AlN})_m/(\text{ScN})_n$ superlattices in which the total number of atomic layers along the b -axis remains constant ($m+n=8$) and vary the number of ScN layers n from 1 to 4, resulting in Sc concentrations of 12.5%, 25%, 37.5%, and 50%.

The resulting clamped and piezoelectric contributions to r_{13} and r_{33} are plotted in Fig. 3(b). r_{13} is relatively insensitive to Sc content, but both contributions to r_{33} rapidly increase above $x_{\text{Sc}} = 25\%$. At $m=n=4$, i.e., $x_{\text{Sc}} = 50\%$, the total r_{33} reaches up to 40 pm/V, representing a twenty-fold enhancement over pure AlN and surpassing the EO coefficient of LNO. In Sec. H of the SM, we also study a -plane superlattices with $m=n=1, 2$ and 3 at $x_{\text{Sc}} = 50\%$, and similarly observe enhancements of the EO coefficients.

The reason for the increase in r_{33}^{piezo} is the same as in alloys, namely a substantial piezoelectric coefficient d_{33} combined

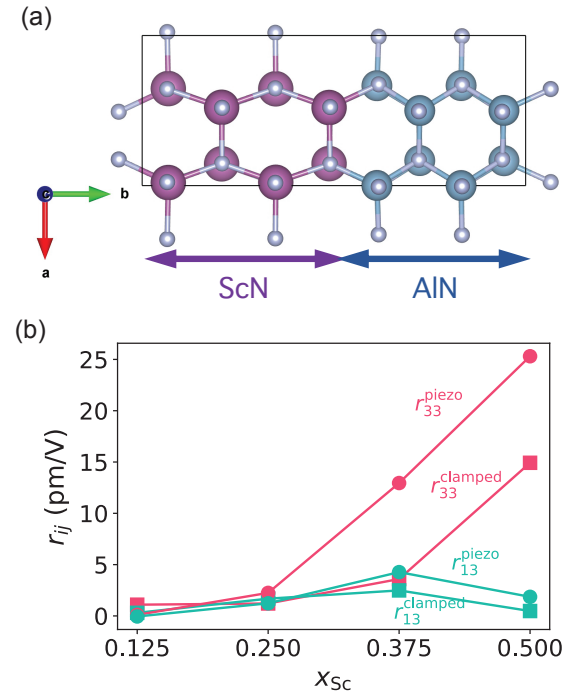


FIG. 3. (a) Atomic structure of an a -plane $(\text{AlN})_m/(\text{ScN})_n$ superlattice with $m = n = 4$ and thus $x_{\text{Sc}} = 50\%$. (b) Clamped and piezoelectric contributions to r_{33} and r_{13} for $x_{\text{Sc}} = n/(m+n)$.

with a large compliance constant S_{33} (see Fig. S8). Interestingly, Fig. 3(b) shows that in the superlattice structures not just r_{33}^{piezo} reaches large values at high Sc content, but also r_{33}^{clamped} . This contrasts with the behavior in $\text{Al}_{1-x}\text{Sc}_x\text{N}$ alloys, where r_{33}^{clamped} always remain modest.

To investigate the origin of the enhancement in r_{33}^{clamped} , we compare r_{33}^{ion} with r_{33}^{elec} in Fig. S9 (Sec. I of the SM) at $x_{\text{Sc}} = 50\%$, showing that the former dominates r_{33}^{clamped} . According to Eq. (2), we decompose r_{33}^{ion} mode-by-mode into the Raman susceptibility α_{33}^m and the mode polarity $l_{m,3}$. For 32-atom superlattices, 96 phonon modes (3 acoustic and 93 optical modes) are analyzed in Fig. S10. At 50%, two phonon modes, in which AlN and ScN layers moving towards opposite directions along c , contribute most strongly to the EO response. These two shearing modes have large Raman susceptibility α_{33}^m and mode polarity $l_{m,3}$ at low frequencies (139 and 254 cm^{-1}), leading to the substantial ionic EO contributions to r_{33}^{clamped} .

In summary, we have reported first-principles investigations of the EO effect in $\text{Al}_{1-x}\text{Sc}_x\text{N}$ alloys and a -plane $(\text{AlN})_m/(\text{ScN})_n$ superlattices. For alloys, we find that the piezoelectric contributions r_{33}^{piezo} dominate over r_{33}^{clamped} at x_{Sc} above 30%. We identify that r_{33}^{piezo} is enhanced by cation ordering that weakens the cation-nitrogen bonds along the c axis, resulting in large compliance constants S_{33} . We find that in-plane strains can dramatically increase r_{33}^{piezo} by driving the system closer to the phase transition. Non-polar a -plane

(AlN)_{*m*}/(ScN)_{*n*} superlattices can also be used to significantly enhance both clamped and piezoelectric contributions to r_{33} . The insights provided by our work provide guidelines for synthesizing Al_{1-x}Sc_{*x*}N alloys and heterostructures with optimized electro-optic coefficients.

See the Supplementary Material for the sensitivity of EO coefficients to the choice of functional, lattice geometries, the symmetry of EO tensor and variations of r_{33} in Al_{1-x}Sc_{*x*}N alloys, bond strength evaluation of random and cation-ordered structures, independence of conclusions for strained structures on alloy configuration, decomposition of r_{33} in the presence of strain, and the EO coefficients of *a*-plane (AlN)_{*m*}/(ScN)_{*n*} superlattices.

ACKNOWLEDGMENTS

The authors appreciate fruitful discussions with Profs. C. Dreyer, H. Tang, F. Rana, and D. Jena. This work is supported by the Army Research Office (W911NF-22-1-0139) and by SUPREME, one of seven centres in JUMP 2.0, a Semiconductor Research Corporation program sponsored by the Defense Advanced Research Projects Agency. This work used Bridges-2 at Pittsburgh Supercomputing Center (PSC) through allocation DMR070069 from the Advanced Cyber-infrastructure Coordination Ecosystem: Services & Support (ACCESS) program, which is supported by National Science Foundation grant No. 2138259, 2138286, 2138307, 2137603 and 2138296. This research also used resources of the National Energy Research Scientific Computing Center, a DOE Office of Science User Facility supported by the Office of Science of the U.S. Department of Energy under Contract No. DE-AC02-05CH11231 using NERSC award BES-ERCAP0028497.

AUTHOR DECLARATIONS

Conflict of Interest

The authors have no conflicts to disclose.

DATA AVAILABILITY

The data that support the findings of this study are available from the corresponding author upon reasonable request.

- ¹Y. Pu, R. Grange, C.-L. Hsieh, and D. Psaltis, “Nonlinear optical properties of core-shell nanocavities for enhanced second-harmonic generation,” *Phys. Rev. Lett.* **104**, 207402 (2010).
- ²R. Boyd and D. Prato, *Nonlinear Optics* (Elsevier Science, 2008).
- ³G. T. Reed, G. Mashanovich, F. Y. Gardes, and D. Thomson, “Silicon optical modulators,” *Nat. Photonics* **4**, 518–526 (2010).
- ⁴M. J. Heck, H.-W. Chen, A. W. Fang, B. R. Koch, D. Liang, H. Park, M. N. Sysak, and J. E. Bowers, “Hybrid silicon photonics for optical interconnects,” *IEEE J. Sel. Top. Quantum Electron.* **17**, 333–346 (2010).
- ⁵M. Li and H. X. Tang, “Strong pockels materials,” *Nat. Mater.* **18**, 9–11 (2019).

- ⁶A. F. Benner, M. Ignatowski, J. A. Kash, D. M. Kuchta, and M. B. Ritter, “Exploitation of optical interconnects in future server architectures,” *IBM J. Res. Dev.* **49**, 755–775 (2005).
- ⁷L. Fan, C.-L. Zou, R. Cheng, X. Guo, X. Han, Z. Gong, S. Wang, and H. X. Tang, “Superconducting cavity electro-optics: a platform for coherent photon conversion between superconducting and photonic circuits,” *Sci. Adv.* **4**, eaar4994 (2018).
- ⁸T. P. McKenna, J. D. Witmer, R. N. Patel, W. Jiang, R. Van Laer, P. Arrangoiz-Arriola, E. A. Wollack, J. F. Herrmann, and A. H. Safavi-Naeini, “Cryogenic microwave-to-optical conversion using a triply resonant lithium-niobate-on-sapphire transducer,” *Optica* **7**, 1737–1745 (2020).
- ⁹R. Luo, H. Jiang, S. Rogers, H. Liang, Y. He, and Q. Lin, “On-chip second-harmonic generation and broadband parametric down-conversion in a lithium niobate microresonator,” *Opt. Express* **25**, 24531–24539 (2017).
- ¹⁰J.-Y. Chen, Z.-H. Ma, Y. M. Sua, Z. Li, C. Tang, and Y.-P. Huang, “Ultra-efficient frequency conversion in quasi-phase-matched lithium niobate microresonators,” *Optica* **6**, 1244–1245 (2019).
- ¹¹A. W. Bruch, X. Liu, J. B. Surya, C.-L. Zou, and H. X. Tang, “On-chip $\chi^{(2)}$ microresonator optical parametric oscillator,” *Optica* **6**, 1361–1366 (2019).
- ¹²S. Abel, T. Stöferle, C. Marchiori, C. Rossel, M. D. Rossell, R. Erni, D. Caimi, M. Sousa, A. Chelnokov, B. J. Offrein, *et al.*, “A strong electro-optically active lead-free ferroelectric integrated on silicon,” *Nat. Commun.* **4**, 1671 (2013).
- ¹³D. Janner, D. Tulli, M. García-Granda, M. Belmonte, and V. Pruneri, “Micro-structured integrated electro-optic LiNbO₃ modulators,” *Laser Photonics Rev.* **3**, 301–313 (2009).
- ¹⁴F. Eltes, C. Mai, D. Caimi, M. Kroh, Y. Popoff, G. Winzer, D. Petousi, S. Lischke, J. E. Ortmann, L. Czornomaz, *et al.*, “A BaTiO₃-based electro-optic Pockels modulator monolithically integrated on an advanced silicon photonics platform,” *J. Light. Technol.* **37**, 1456–1462 (2019).
- ¹⁵T. Paoletta and A. A. Demkov, “Pockels effect in low-temperature rhombohedral BaTiO₃,” *Phys. Rev. B* **103**, 014303 (2021).
- ¹⁶Z. Jiang, C. Paillard, H. Xiang, and L. Bellaïche, “Linear versus nonlinear electro-optic effects in materials,” *Phys. Rev. Lett.* **125**, 017401 (2020).
- ¹⁷C. Paillard, S. Prokhorenko, and L. Bellaïche, “Strain engineering of electro-optic constants in ferroelectric materials,” *Npj Comput. Mater.* **5**, 6 (2019).
- ¹⁸B. Dong, X. Luo, S. Zhu, M. Li, D. Hasan, L. Zhang, S. J. Chua, J. Wei, Y. Chang, G.-Q. Lo, *et al.*, “Aluminum nitride on insulator (AlNOI) platform for mid-infrared photonics,” *Opt. Lett.* **44**, 73–76 (2019).
- ¹⁹W. H. Pernice, C. Xiong, C. Schuck, and H. Tang, “High-Q aluminum nitride photonic crystal nanobeam cavities,” *Appl. Phys. Lett.* **100** (2012).
- ²⁰W. H. Pernice, C. Xiong, and H. X. Tang, “High Q micro-ring resonators fabricated from polycrystalline aluminum nitride films for near infrared and visible photonics,” *Opt. Express* **20**, 12261–12269 (2012).
- ²¹C. Xiong, W. H. Pernice, and H. X. Tang, “Low-loss, silicon integrated, aluminum nitride photonic circuits and their use for electro-optic signal processing,” *Nano Lett.* **12**, 3562–3568 (2012).
- ²²E. L. Wooten, K. M. Kissa, A. Yi-Yan, E. J. Murphy, D. A. Lafaw, P. F. Hallemeier, D. Maack, D. V. Attanasio, D. J. Fritz, G. J. McBrien, *et al.*, “A review of lithium niobate modulators for fiber-optic communications systems,” *IEEE J. Sel. Top. Quantum Electron.* **6**, 69–82 (2000).
- ²³V. Yoshioka, J. Lu, Z. Tang, J. Jin, R. H. Olsson, and B. Zhen, “Strongly enhanced second-order optical nonlinearity in cmos-compatible Al_{1-x}Sc_{*x*}N thin films,” *APL Mater.* **9** (2021).
- ²⁴M. Akiyama, K. Kano, and A. Teshigahara, “Influence of growth temperature and scandium concentration on piezoelectric response of scandium aluminum nitride alloy thin films,” *Appl. Phys. Lett.* **95** (2009).
- ²⁵R. Matloub, M. Hadad, A. Mazzalai, N. Chidambaram, G. Moulard, C. Sandu, T. Metzger, and P. Muralt, “Piezoelectric Al_{1-x}Sc_{*x*}N thin films: A semiconductor compatible solution for mechanical energy harvesting and sensors,” *Appl. Phys. Lett.* **102** (2013).
- ²⁶S. Fichtner, N. Wolff, F. Lofink, L. Kienle, and B. Wagner, “Alsen: A III-V semiconductor based ferroelectric,” *J. Appl. Phys.* **125** (2019).
- ²⁷H. Wang, N. Adamski, S. Mu, and C. G. Van de Walle, “Piezoelectric effect and polarization switching in Al_{1-x}Sc_{*x*}N,” *J. Appl. Phys.* **130** (2021).
- ²⁸D. Hamann, “Optimized norm-conserving Vanderbilt pseudopotentials,” *Phys. Rev. B* **88**, 085117 (2013).
- ²⁹X. Gonze, “A brief introduction to the ABINIT software package,” *Z. Kristallogr. Cryst. Mater.* **220**, 558–562 (2005).

³⁰M. Veithen, X. Gonze, and P. Ghosez, “Nonlinear optical susceptibilities, raman efficiencies, and electro-optic tensors from first-principles density functional perturbation theory,” *Phys. Rev. B* **71**, 125107 (2005).

³¹D. M. Ceperley and B. J. Alder, “Ground state of the electron gas by a stochastic method,” *Phys. Rev. Lett.* **45**, 566 (1980).

³²J. P. Perdew and A. Zunger, “Self-interaction correction to density-functional approximations for many-electron systems,” *Phys. Rev. B* **23**, 5048 (1981).

³³A. V. Krukau, O. A. Vydrov, A. F. Izmaylov, and G. E. Scuseria, “Influence of the exchange screening parameter on the performance of screened hybrid functionals,” *J. Chem. Phys.* **125**, 224106 (2006).

³⁴The lattice vectors in the primitive cell of wurtzite AlN are $\mathbf{a} = a_0(\frac{\sqrt{3}}{2}, \frac{1}{2}, 0)$, $\mathbf{b} = a_0(-\frac{\sqrt{3}}{2}, \frac{1}{2}, 0)$ and $\mathbf{c} = c_0(0, 0, 1)$. An orthorhombic 8-atom conventional unit cell is constructed with lattice vectors $\mathbf{a}' = \mathbf{a} + \mathbf{b}$, $\mathbf{b}' = \mathbf{a} - \mathbf{b}$ and $\mathbf{c}' = \mathbf{c}$.

³⁵H. J. Monkhorst and J. D. Pack, “Special points for brillouin-zone integrations,” *Phys. Rev. B* **13**, 5188 (1976).

³⁶We use the symbol $l_{m,k}$ for mode polarity, rather than the more customary $p_{m,k}$, to avoid confusion with the elasto-optic coefficients.

³⁷M. Akiyama, T. Kamohara, K. Kano, A. Teshigahara, Y. Takeuchi, and N. Kawahara, “Enhancement of piezoelectric response in scandium aluminum nitride alloy thin films prepared by dual reactive cosputtering,” *Adv. Mater.* **21**, 593–596 (2009).

³⁸G. Schönweger, A. Petraru, M. R. Islam, N. Wolff, B. Haas, A. Hammud, C. Koch, L. Kienle, H. Kohlstedt, and S. Fichtner, “From fully strained to relaxed: Epitaxial ferroelectric $\text{Al}_{1-x}\text{Sc}_x\text{N}$ for III-N technology,” *Adv. Funct. Mater.* **32**, 2109632 (2022).

³⁹S. Satoh, K. Ohtaka, T. Shimatsu, and S. Tanaka, “Crystal structure deformation and phase transition of AlScN thin films in whole sc concentration range,” *J. Appl. Phys.* **132**, 025103 (2022).

⁴⁰R. Dronskowski and P. E. Bloechl, “Crystal orbital hamilton populations (COHP): energy-resolved visualization of chemical bonding in solids based on density-functional calculations,” *J. Phys. Chem.* **97**, 8617–8624 (1993).

⁴¹S. Maintz, V. L. Deringer, A. L. Tchougréeff, and R. Dronskowski, “LOBSTER: A tool to extract chemical bonding from plane-wave based DFT,” *J. Comput. Chem.* **37**, 1030–1035 (2016).

⁴²The critical strain is determined by a sign reversal of the compliance constant S_{33} which represents the yield point, i.e., the transition from elastic to plastic deformation. S_{33} goes from plus-infinity to minus-infinity across the critical strain.

⁴³J. Casamento, H. Lee, T. Maeda, V. Gund, K. Nomoto, L. van Deurzen, W. Turner, P. Fay, S. Mu, C. G. Van de Walle, A. Lal, H. G. Xing, and D. Jena, “Epitaxial $\text{Sc}_x\text{Al}_{1-x}\text{N}$ on GaN exhibits attractive high-K dielectric properties,” *Appl. Phys. Lett.* **120**, 152901 (2022).

⁴⁴M. Park, Z. Hao, R. Dargis, A. Clark, and A. Ansari, “Epitaxial aluminum scandium nitride super high frequency acoustic resonators,” *J. Microelectromechanical Syst.* **29**, 490–498 (2020).

⁴⁵A. K. Hamze and A. A. Demkov, “First-principles study of the linear electro-optical response in strained SrTiO_3 ,” *Phys. Rev. Mater.* **2**, 115202 (2018).

⁴⁶S. Kondo, T. Yamada, A. K. Tagantsev, P. Ma, J. Leuthold, P. Martelli, P. Boffi, M. Martinelli, M. Yoshino, and T. Nagasaki, “Large impact of strain on the electro-optic effect in $(\text{Ba}, \text{Sr})\text{TiO}_3$ thin films: Experiment and theoretical comparison,” *Appl. Phys. Lett.* **115**, 092901 (2019).

⁴⁷B. Chmielak, M. Waldow, C. Mattheisen, C. Ripperda, J. Bolten, T. Wahlbrink, M. Nagel, F. Merget, and H. Kurz, “Pockels effect based fully integrated, strained silicon electro-optic modulator,” *Opt. Express* **19**, 17212–17219 (2011).

⁴⁸R. S. Jacobsen, K. N. Andersen, P. I. Borel, J. Fage-Pedersen, L. H. Frandsen, O. Hansen, M. Kristensen, A. V. Lavrinenko, G. Moulin, H. Ou, C. Peucheret, B. Zsigri, and A. Bjarklev, “Strained silicon as a new electro-optic material,” *Nature* **441**, 199–202 (2006).

⁴⁹Z. Jiang, C. Paillard, D. Vanderbilt, H. Xiang, and L. Bellaiche, “Designing multifunctionality via assembling dissimilar materials: Epitaxial AlN/ScN superlattices,” *Phys. Rev. Lett.* **123**, 096801 (2019).

⁵⁰For comparison, we also investigated c -plane superlattices (which do not have the ordering along the c axis); we observed no enhancements of EO coefficients.

Supplementary Material for “Towards higher electro-optic response in AlScN”

Haochen Wang,¹ Sai Mu,² and Chris G. Van de Walle¹

¹⁾*Materials Department, University of California Santa Barbara, Santa Barbara, CA 93106-5050, USA*

²⁾*Department of Physics and Astronomy, University of South Carolina, Columbia, SC 29208, USA*

(*Electronic mail: vandewalle@mrl.ucsb.edu)

(*Electronic mail: mus@mailbox.sc.edu)

(Dated: 11 October 2024)

A. Sensitivity of electro-optic coefficients to the choice of functional

We use the local density approximation (LDA) as the exchange-correlation functional in our density functional theory (DFT) calculations. LDA underestimates the band gap of semiconductors and insulators; here we test to what extent this could affect our results for electro-optic (EO) coefficients.

EO coefficients have contributions from electronic, ionic, and piezoelectric responses. According to Eqs. (2) and (5) in the main text, each contribution includes at least one variable that could be affected by the band gap, including dielectric permittivity ϵ_{ij} , nonlinear optical susceptibility $d_{ij} = \frac{1}{2}\chi_{ij}^{(2)}$, Raman susceptibility α_{ij}^m , and elasto-optic coefficients p_{ij} . To assess the impact of the band gap on these properties, we apply a scissor correction which adjusts the conduction-band energies such that the band gap matches the experimental value.

We use AlN and $\text{Al}_{0.5}\text{Sc}_{0.5}\text{N}$ in primitive cells as examples, with LDA-calculated band gaps of 4.38 and 3.25 eV, respectively. To adjust the gap to experimental values,^{1,2} scissor corrections of 1.65 eV for AlN and 1.25 eV for $\text{Al}_{0.5}\text{Sc}_{0.5}\text{N}$ are applied. Table I presents a comparison of various properties calculated using LDA and the “LDA + scissor correction” approach.

In pure AlN, the ionic contribution r_{13}^{ion} dominates the total EO coefficient. Adjusting the band gap reduces r_{13}^{total} by 10% and r_{33}^{total} by 17%. In $\text{Al}_{0.5}\text{Sc}_{0.5}\text{N}$, the band-gap correction reduces r_{13}^{elec} and r_{13}^{ion} , but increases r_{13}^{piezo} , leading to a compensation in correction terms and reductions of r_{13}^{total} by only 7% and r_{33}^{total} by only 11%. Our tests thus indicate that adjusting the band gap changes the total EO coefficients by less than 17%. We conclude that corrections to the EO coefficients due to the LDA underestimation of the band gap are relatively modest and will not affect our conclusions.

TABLE I. Comparison of various properties of AlN and $\text{Al}_{0.5}\text{Sc}_{0.5}\text{N}$ calculated by LDA and with scissor correction. ϵ_{ij} and α_{ij} are dielectric permittivity and Raman susceptibility. d_{ij} (pm/V), p_{ij} , r_{ij} (pm/V) represent the nonlinear optical susceptibility, elasto-optic coefficients and EO coefficients in Voigt notation. The electronic, ionic and piezoelectric contributions of the EO coefficients are listed separately .

	AlN		$\text{Al}_{0.5}\text{Sc}_{0.5}\text{N}$	
	LDA	Scissor	LDA	Scissor
$\epsilon_{11}^{\text{elec}}$	4.393	3.888	5.883	5.136
$\epsilon_{33}^{\text{elec}}$	4.563	4.017	5.861	5.113
α_{11}^m	-0.003	-0.002	0.007	0.005
α_{33}^m	0.006	0.004	0.003	0.002
d_{13}	-0.017	0.010	-13.346	-8.102
d_{33}	-4.069	-2.655	-0.027	1.406
p_{11}	-0.069	-0.059	-0.012	-0.015
p_{12}	-0.055	-0.043	0.011	0.022
p_{13}	-0.083	-0.075	0.014	0.024
p_{31}	-0.026	-0.017	-0.021	-0.015
p_{33}	-0.120	-0.104	0.028	0.038
p_{55}	-0.062	-0.068	-0.075	-0.088
r_{13}^{elec}	0.003	-0.002	1.542	1.229
r_{33}^{elec}	0.782	0.658	0.003	-0.215
r_{13}^{ion}	-0.735	-0.631	0.878	0.740
r_{33}^{ion}	1.516	1.301	0.269	0.061
r_{13}^{piezo}	-0.193	-0.197	0.529	0.780
r_{33}^{piezo}	-0.593	-0.541	1.625	1.851
r_{13}^{total}	-0.925	-0.830	2.949	2.749
r_{33}^{total}	1.705	1.418	1.897	1.697

B. Lattice parameters of $\text{Al}_{1-x}\text{Sc}_x\text{N}$ alloys

Results for structural parameters of $\text{Al}_{1-x}\text{Sc}_x\text{N}$ alloys are shown in Fig. S1. As stated in the main text, we randomly generate ten configurations at each Sc concentration and compute the averaged lattice parameters, labeled as “Random” in Fig. S1. We also generate eight cation-ordered structures at each Sc concentration, again computing averages, labeled as “Cation-Ordered”. Figure S1 illustrates that in random alloys the phase transition from wurtzite to layered-hexagonal occurs between 37.5% and 43.75% Sc concentration. In contrast, the cation-ordered structures stay wurtzite even at 43.75% and 50% Sc concentrations.

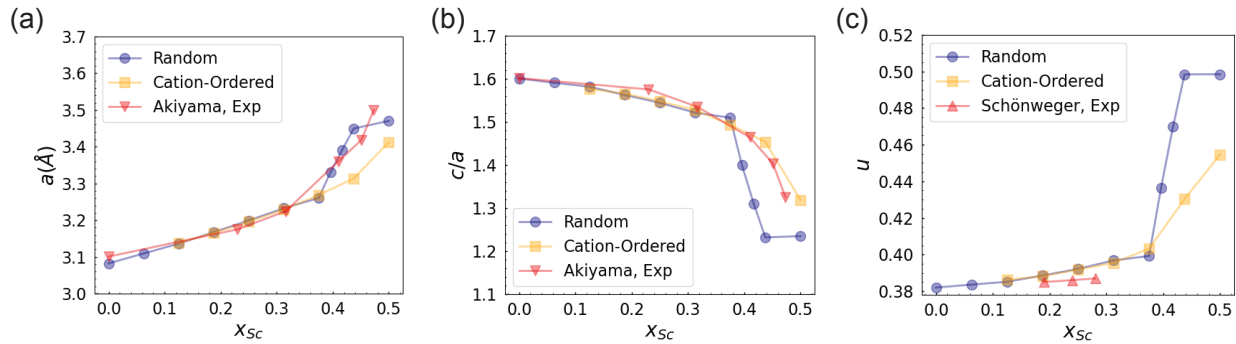


FIG. S1. (a) Lattice parameter a , (b) c/a ratio and (c) internal displacement parameter u as a function of Sc concentration in $\text{Al}_{1-x}\text{Sc}_x\text{N}$ alloys. Blue points represent averages over ten random configurations, while orange points represent averages over cation-ordered structures. Experimental values of a and c/a are from Akiyama *et al.*,³ while experimental u values are from Schönweger *et al.*.⁴

C. Components of the EO tensor of random AlScN alloys

Wurtzite AlN has $6mm$ point group symmetry, which specifies that there should be only three independent non-zero components in the EO tensor, namely r_{13} , r_{33} and r_{51} . The EO tensor in Voigt notation then has the following form:

$$r_{hk} = \begin{pmatrix} 0 & 0 & r_{13} \\ 0 & 0 & r_{13} \\ 0 & 0 & r_{33} \\ 0 & r_{51} & 0 \\ r_{51} & 0 & 0 \\ 0 & 0 & 0 \end{pmatrix} \quad (1)$$

However, the supercells used for modeling AlScN alloys do not necessarily have the full wurtzite symmetry and can hence produce non-zero values for components such as r_{11} and r_{22} . In Fig. S2, we plot the clamped EO coefficients r_{11}^{clamped} and r_{22}^{clamped} . We observe that these values are non-zero, and the variations of r_{22}^{clamped} are mostly larger than r_{11}^{clamped} . The difference may attribute to the anisotropy of a direction (armchair) and b direction (zigzag). Potentially it is *possible* to form the mirror plane perpendicular to the b axis but it's *impossible* to form a mirror plane which is perpendicular to the a axis. This potential mirror symmetry with $m \perp b$ makes the r_{22}^{clamped} very close to zero, compared to r_{11}^{clamped} . But in general they are small and tend to be zero when averaging over all configurations at each Sc concentration.

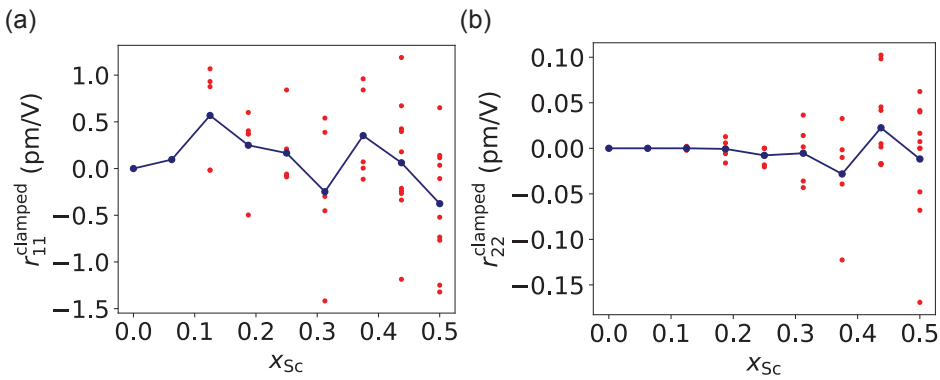


FIG. S2. Clamped EO coefficients (a) r_{11}^{clamped} and (b) r_{22}^{clamped} of random AlScN alloys as a function of Sc concentration. The red points represent different configurations at each Sc concentration; the blue curve denotes averages over the multiple configurations at each Sc concentration.

D. Variations of r_{33} among different configurations of random alloys

In $\text{Al}_{1-x}\text{Sc}_x\text{N}$ random alloys, the variations of both clamped and piezoelectric EO coefficients among different configurations are small at low x_{Sc} but become significant at high x_{Sc} . Figure S3 shows the large variations of r_{33}^{clamped} and r_{33}^{piezo} in random alloys at $x_{\text{Sc}} = 0.5$. Three out of ten configurations have large EO responses. An analysis of pair distribution functions allowed us to identify a common structural feature of alloy configurations that give rise to high EO coefficients: the formation of same-species cation chains along the c axis.

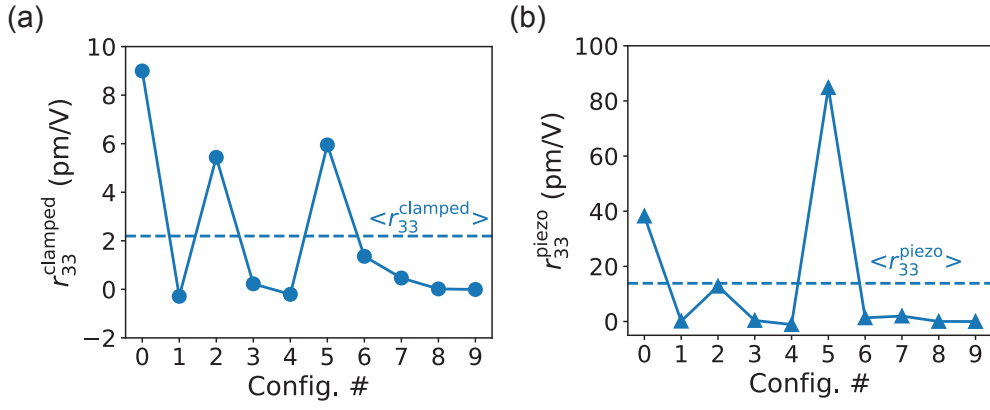


FIG. S3. Clamped (a) and piezoelectric (b) EO coefficients of ten inequivalent configurations of $\text{Al}_{0.5}\text{Sc}_{0.5}\text{N}$ random alloys. The dotted horizontal lines denote averaged values of ten configurations.

E. Bond strength in random and cation-ordered structures

The enhancements of piezoelectric EO coefficients in cation-ordered structures are attributed to the enhanced piezoelectric strain coefficients which further result from the large compliance constants. Large S_{33} in cation-ordered structures reflects weak cation-nitrogen bonds along the c axis. In order to evaluate the bond strength, crystal orbital Hamilton population (COHP) calculations⁵ are performed by employing the LOBSTER software package,⁶ where the integrated COHP (ICOHP) up to the Fermi level serves as an indicator for the bond energy: the more negative values indicate stronger bonds.

We analyze one structure from 32-atom random supercells and another from cation-ordered supercells of $\text{Al}_{0.5}\text{Sc}_{0.5}\text{N}$. Figure S4 shows the bond energies of Al-N and Sc-N bonds along the c axis as a function of bond length. In cation-ordered structures, the magnitude of the averaged ICOHP for Sc–N and Al–N bonds becomes smaller than in random structures, indicating softer cation-nitrogen bonds along the c axis.

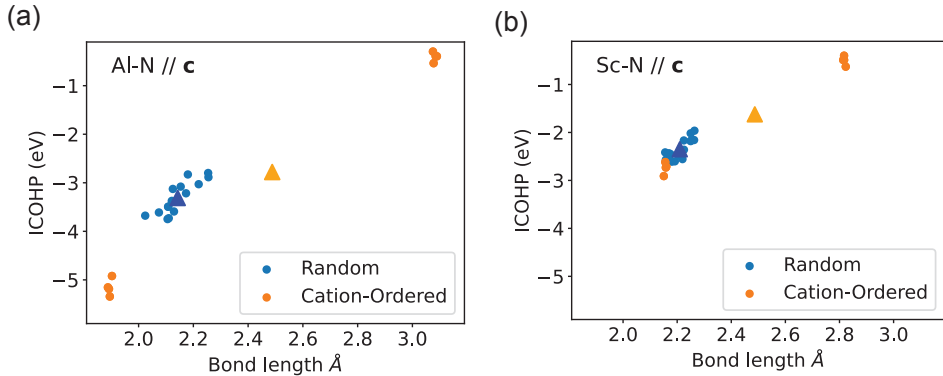


FIG. S4. Integrated (over occupied states) crystal orbital Hamilton populations (ICOHP) for each cation–nitrogen interaction along the c axis in 32-atom Random and Cation-ordered supercells of $\text{Al}_{0.5}\text{Sc}_{0.5}\text{N}$ as a function of bond length: (a) Al–N bonds and (b) Sc–N bonds. Averages are denoted using triangles.

In the case of Al-N bonds, weaker bonding means that the u parameter increases (from its value $u=0.381$ in wurtzite AlN towards the higher value in a layered hexagonal structure). Conversely, in the case of Sc-N bonds, softer bonds decrease u , towards the value in wurtzite. Both effects drive the system closer to the phase transition, which is favorable for enhancing the EO response.

F. Independence of conclusions for strained structures on alloy configuration

Our investigations on the strain effect in the main text are based on one supercell at each Sc concentration of $\text{Al}_{1-x}\text{Sc}_x\text{N}$ alloys. In Fig. S5, we investigate the EO coefficients of five inequivalent configurations of $\text{Al}_{0.8125}\text{Sc}_{0.1875}\text{N}$ as a function of strain. We observe almost identical enhancements in the clamped and piezoelectric EO coefficients as well as in their contributing factors (p_{33} , d_{33} , e_{33} and S_{33}) for the different configurations. We also find that the critical strain is independent of the choice of configuration.

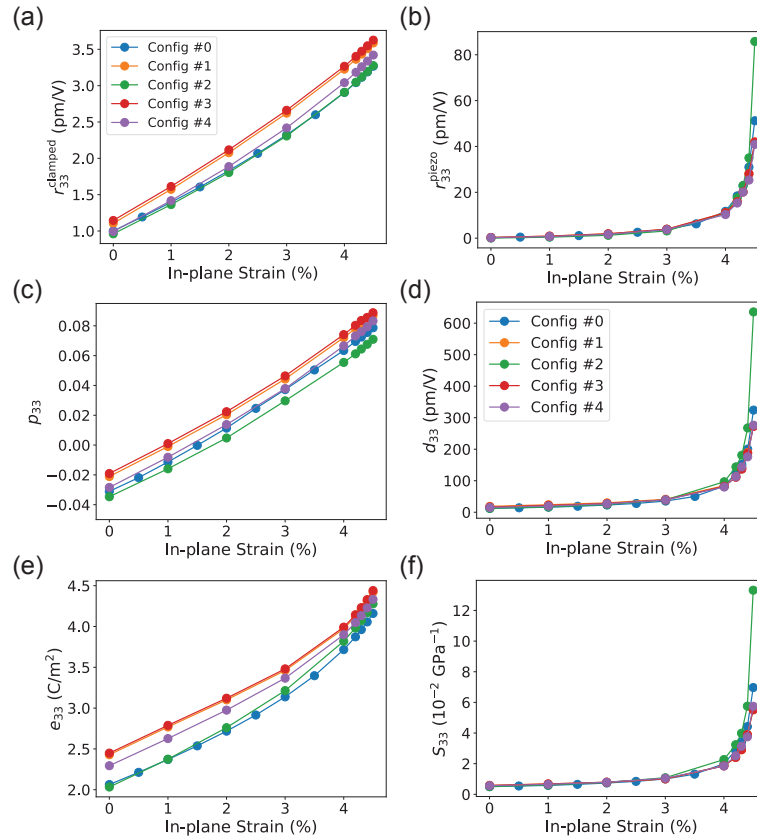


FIG. S5. (a) Clamped EO coefficients r_{33}^{clamped} , (b) piezoelectric EO coefficients r_{33}^{piezo} , (c) elasto-optic coefficients p_{33} , (d) piezoelectric strain coefficients d_{33} , (e) piezoelectric stress coefficients e_{33} and (f) compliance constants S_{33} of $\text{Al}_{0.8125}\text{Sc}_{0.1875}\text{N}$ as a function of in-plane tensile strain.

G. Decomposition of r_{33} in the presence of strain

Figures S6 (a) and (b) show the total and clamped EO coefficients of $\text{Al}_{1-x}\text{Sc}_x\text{N}$ as a function of in-plane strain. In contrast to the dramatic enhancement of r_{33}^{piezo} , r_{33}^{clamped} increases almost linearly without exhibiting divergent behavior when $x_{\text{Sc}} < 43.75\%$.

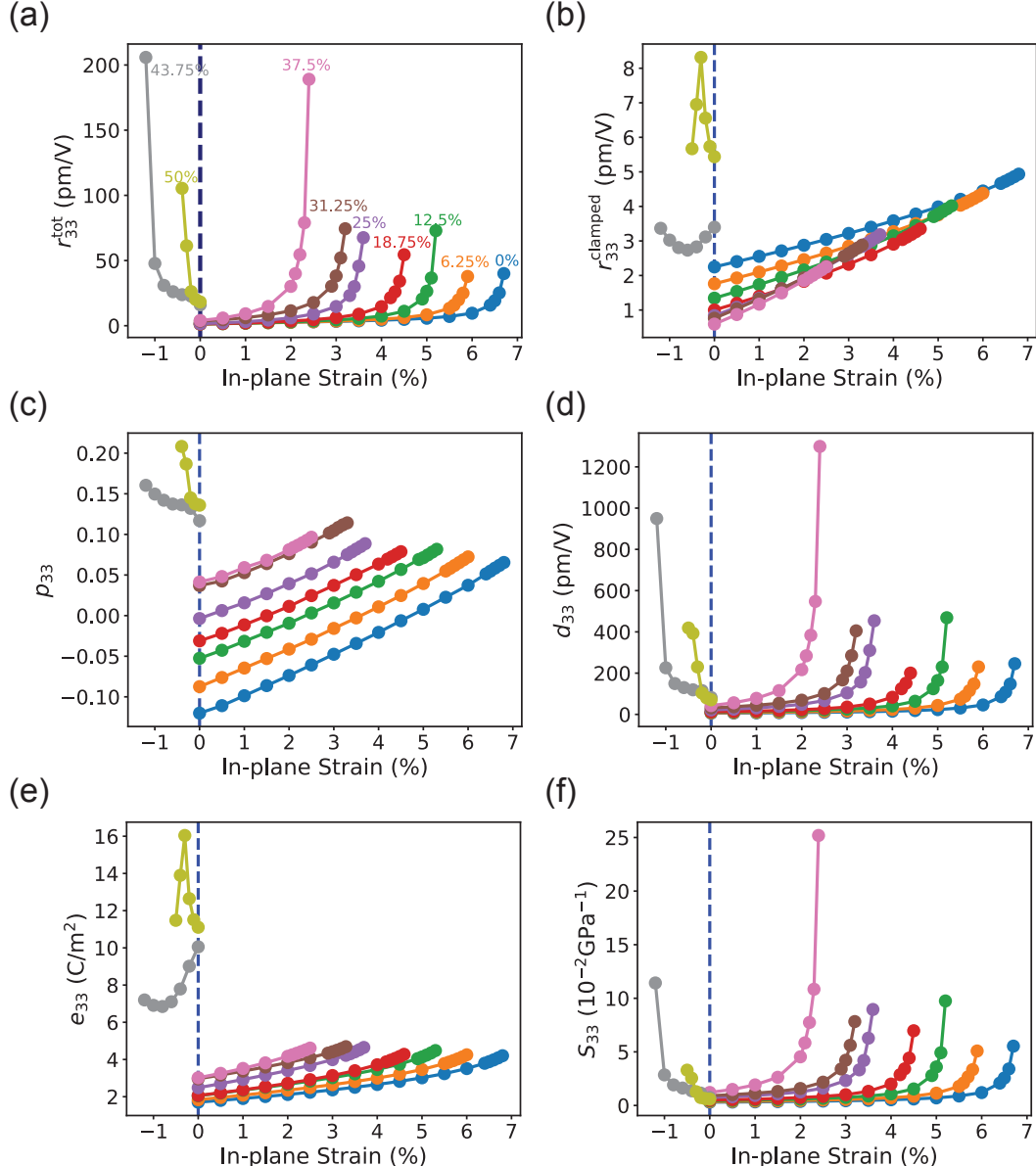


FIG. S6. (a) Total EO coefficients r_{33}^{tot} , (b) Clamped EO coefficients r_{33}^{clamped} , (c) elasto-optic coefficients p_{33} , (d) piezoelectric strain coefficients d_{33} , (e) piezoelectric stress coefficients e_{33} and (f) compliance constants S_{33} of $\text{Al}_{1-x}\text{Sc}_x\text{N}$ alloys as a function of in-plane strain.

Figure S6 (c)-(f) show the factors contributing to r_{33}^{piezo} . The piezoelectric coefficient d_{33} and the compliance constant S_{33} exhibit divergent behavior similar to r_{33}^{piezo} . A critical strain is present at each Sc concentration, decreasing as the Sc concentration increases. As the in-plane strain approaches this critical value, the compliance constant S_{33} increases dramatically, indicating that relatively small stresses can induce very large strain responses. This softening of the material significantly enhances d_{33} , thereby amplifying the piezoelectric contributions to EO coefficients r_{33}^{piezo} .

We note that r_{13}^{piezo} (and its components d_{13} and S_{13}) exhibit similar behavior as a function of strain; see Fig. S7.

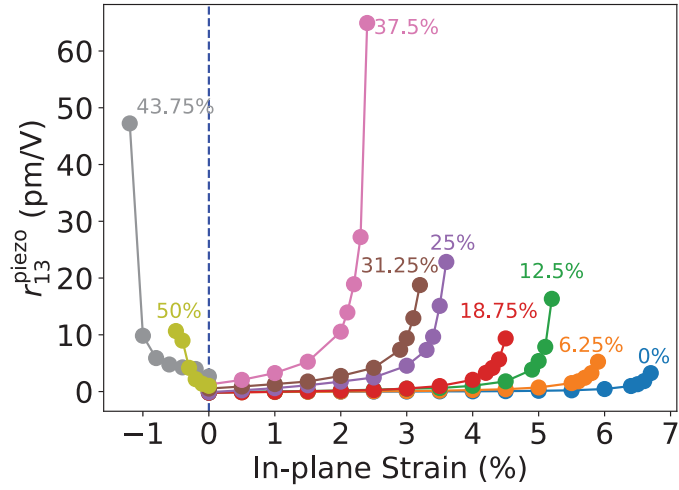


FIG. S7. Piezoelectric contribution to the EO coefficient, r_{13}^{piezo} , for random AlScN alloys as a function of in-plane strain.

H. Electro-optic coefficients of *a*-plane $(\text{AlN})_m/(\text{ScN})_n$ superlattices with $m+n = 2, 4, 6$

In the main text, we construct *a*-plane superlattices with $m+n = 8$ at four different Sc concentrations, $(\text{AlN})_7/(\text{ScN})_1$, $(\text{AlN})_6/(\text{ScN})_2$, $(\text{AlN})_5/(\text{ScN})_3$ and $(\text{AlN})_4/(\text{ScN})_4$, and we observe large enhancements in both clamped and piezoelectric EO coefficients r_{33} at 50% Sc concentration $(\text{AlN})_4/(\text{ScN})_4$.

We have also generated three other *a*-plane superlattices, all at 50% Sc concentration, namely $(\text{AlN})_1/(\text{ScN})_1$, $(\text{AlN})_2/(\text{ScN})_2$ and $(\text{AlN})_3/(\text{ScN})_3$. The clamped and piezoelectric EO coefficients r_{13} and r_{33} are shown in Table II, together with the case of $m = n = 4$. In all four *a*-plane superlattices, the total EO coefficients are enhanced compared to those in random alloys. We observe that superlattices containing an odd number of layers of each material have larger EO coefficients than those containing an even number of layers.

TABLE II. Clamped and piezoelectric EO coefficients r_{13} and r_{33} (pm/V), in four *a*-plane $(\text{AlN})_m/(\text{ScN})_n$ superlattices with $m = n$.

$m = n =$	1	2	3	4
r_{13}^{clamped}	0.03	2.24	0.58	0.48
r_{13}^{piezo}	6.66	4.60	7.39	1.72
r_{33}^{clamped}	4.23	3.42	8.28	14.92
r_{33}^{piezo}	71.89	15.45	27.88	23.10

I. Analysis of electro-optic coefficients of *a*-plane $(\text{AlN})_m/(\text{ScN})_n$ superlattices with $m+n=8$

In *a*-plane $(\text{AlN})_m/(\text{ScN})_n$ superlattices, both clamped and piezoelectric contributions to r_{33} are enhanced with an increase of ScN layers. At 50% Sc concentration, the total EO coefficient r_{33} goes up to 41 pm/V. In contrast to what we observed in $\text{Al}_{1-x}\text{Sc}_x\text{N}$ alloys, in *a*-plane superlattices clamped contributions rise with Sc concentration and are comparable to piezoelectric contributions even at high Sc concentrations.

To explain why *a*-plane superlattices exhibit large piezoelectric EO coefficients at high Sc concentrations, the contributing terms to r_{33}^{piezo} and r_{13}^{piezo} are plotted in Fig. S8. According to Eqs. (5) and (6) of the main text, the piezoelectric EO coefficients are derived from elasto-optic coefficients and piezoelectric strain coefficients, with the latter decomposed further into piezoelectric stress coefficients e_{ik} and the compliance tensor S_{kj} . From Fig. S8(a), we observe that the elasto-optic coefficients p_{33} significantly increase at higher Sc concentrations. Additionally, the piezoelectric strain coefficients d_{33} [Fig. S8(b)] are notably high at 37.5% and 50% x_{Sc} . Combining these two factors, *a*-plane superlattices achieve large piezoelectric EO coefficients r_{33}^{piezo} at higher concentrations.

The electronic and ionic contributions to the clamped EO coefficients r_{33}^{clamped} are plotted in Fig. S9. The ionic response dominates the clamped EO coefficients, overshadowing electronic contributions, particularly at 50% concentration.

To elucidate the enhancement in the ionic contribution, we analyze r_{33}^{ion} through mode-by-mode decomposition in Fig. S10. Given the use of 32-atom supercells, 96 phonon modes are included in the analysis. At 50%, two shearing phonon modes, in which AlN and ScN layers move along *c* in opposite directions, significantly contribute to the ionic response: mode 6 with relatively small Raman susceptibility and mode polarity but very low phonon frequency (139 cm^{-1}); and mode 16 with large Raman susceptibility and mode polarity but slightly higher phonon frequency (254 cm^{-1}).

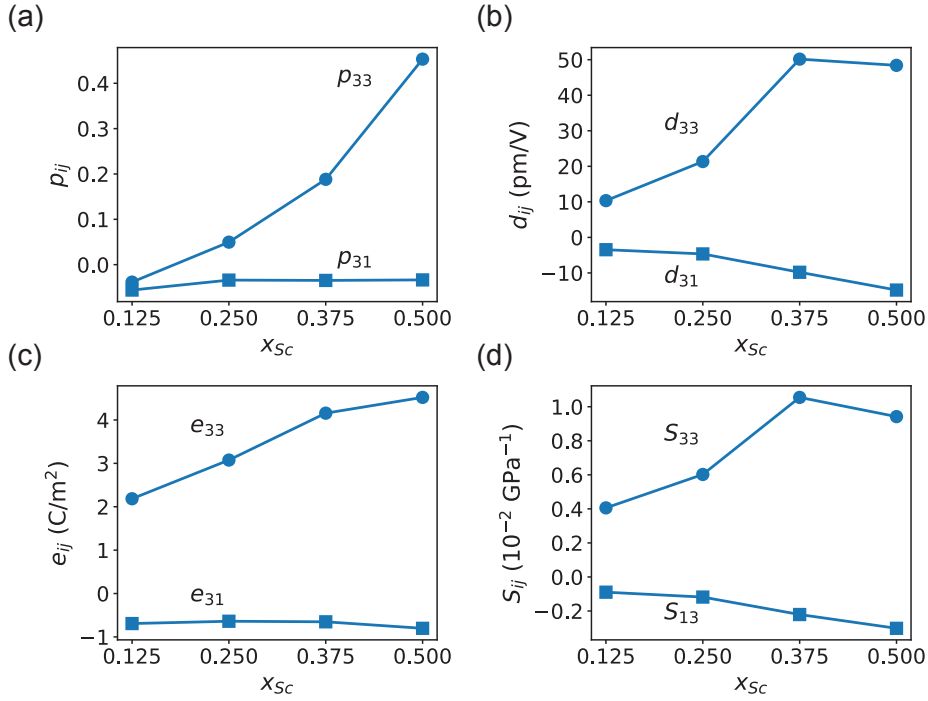


FIG. S8. (a) Elasto-optic coefficients p_{ij} , (b) piezoelectric strain coefficients d_{ij} , (c) piezoelectric stress coefficients e_{ij} and (d) compliance constants S_{ij} of a -plane superlattices $(\text{AlN})_m/(\text{ScN})_n$ as a function of $x_{Sc} = n/(m+n)$.

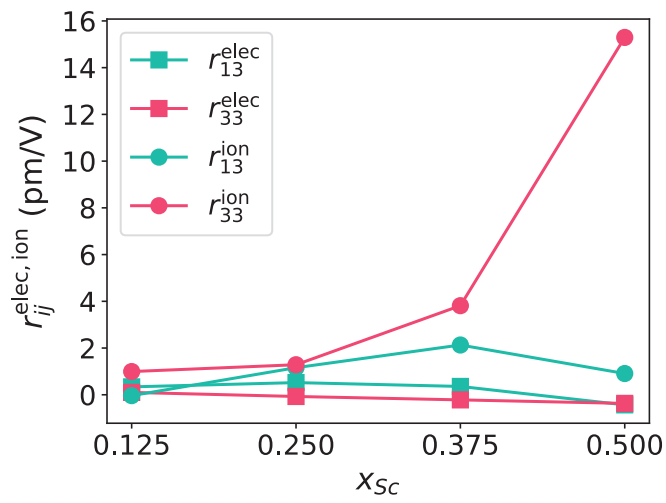


FIG. S9. Ionic and electronic EO contributions r_{33} and r_{13} of a -plane superlattices $(\text{AlN})_m/(\text{ScN})_n$.

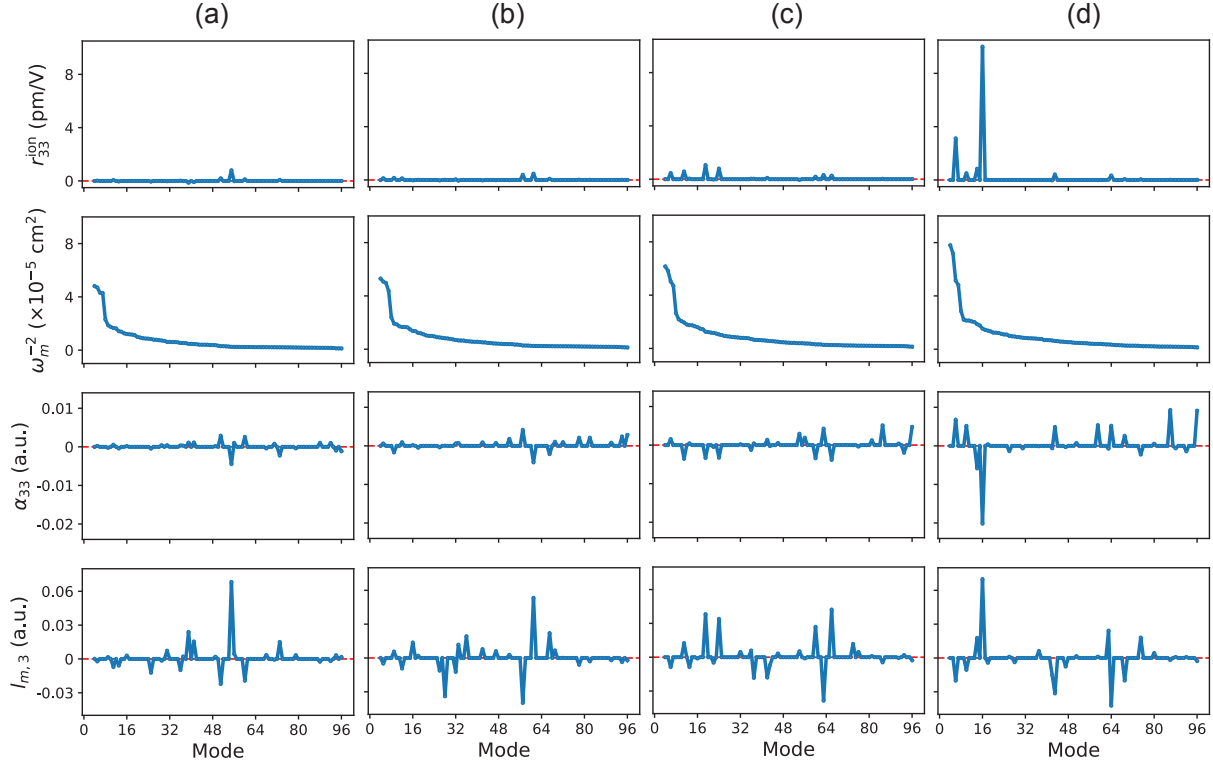


FIG. S10. Mode-by-mode decompositions of r_{33}^{ion} for a -plane superlattices $(\text{AlN})_m/(\text{ScN})_n$ at (a) 12.5%, (b) 25%, (c) 37.5% and (d) 50% Sc concentrations. At each concentration, the panels show (from top to bottom) the ionic EO coefficient contributed by mode m , the frequency-dependent factor ω_m^{-2} , the Raman susceptibility α_{33}^m , and the mode polarity $l_{m,3}$.

REFERENCES

¹Q. G. Q. Guo and A. Y. A. Yoshida, “Temperature dependence of band gap change in InN and AlN,” *Jpn. J. Appl. Phys.* **33**, 2453 (1994).

²M. Baeumler, Y. Lu, N. Kurz, L. Kirste, M. Prescher, T. Christoph, J. Wagner, A. Žukauskaitė, and O. Ambacher, “Optical constants and band gap of wurtzite $\text{Al}_{1-x}\text{Sc}_x\text{N}/\text{Al}_2\text{O}_3$ prepared by magnetron sputter epitaxy for scandium concentrations up to $x=0.41$,” *J. Appl. Phys.* **126**, 045715 (2019).

³M. Akiyama, T. Kamohara, K. Kano, A. Teshigahara, Y. Takeuchi, and N. Kawahara, “Enhancement of piezoelectric response in scandium aluminum nitride alloy thin films prepared by dual reactive cosputtering,” *Adv. Mater.* **21**, 593–596 (2009).

⁴G. Schönweger, A. Petraru, M. R. Islam, N. Wolff, B. Haas, A. Hammud, C. Koch, L. Kienle, H. Kohlstedt, and S. Fichtner, “From fully strained to relaxed: Epitaxial ferroelectric $\text{Al}_{1-x}\text{Sc}_x\text{N}$ for III-N technology,” *Adv. Funct. Mater.* **32**, 2109632 (2022).

⁵R. Dronskowski and P. E. Bloechl, “Crystal orbital hamilton populations (COHP): energy-resolved visualization of chemical bonding in solids based on density-functional calculations,” *J. Phys. Chem.* **97**, 8617–8624 (1993).

⁶S. Maintz, V. L. Deringer, A. L. Tchougréeff, and R. Dronskowski, “LOBSTER: A tool to extract chemical bonding from plane-wave based DFT,” *J. Comput. Chem.* **37**, 1030–1035 (2016).